Chemical Science

ROYAL SOCIETY OF CHEMISTRY

EDGE ARTICLE

View Article Online
View Journal | View Issue

Cite this: *Chem. Sci.*, 2025, **16**, 16904

All publication charges for this article have been paid for by the Royal Society of Chemistry

A biomimetic supramolecular platform enables sequential four-step energy transfer and reactive oxygen species modulation for selective photocatalytic oxidations

Yu-Song Bi, Wen-Qiang Liu, * Hui Liu and Ling-Bao Xing *

Natural photosynthesis, a quintessential energy conversion process sustaining life on Earth through its sophisticated multi-step energy transfer cascades, has inspired the development of artificial light-harvesting systems aimed at mimicking its efficiency and complexity. Here, we report a supramolecular energy transfer platform constructed *via* electrostatic interactions between sodium polystyrene sulfonate (RSS) and a quaternary ammonium salt modified cyano-substituted phenylenevinylene derivative (PPTA) in H_2O medium, achieving a sequential four-step energy relay. Energy is sequentially transferred from the PPTA-RSS complex to eosin Y (EY), rhodamine B (RhB), sulforhodamine 101 (SR101), and cyanine 5 (Cy5), with stepwise enhancement in superoxide anion radical ($O_2^{\bullet-}$) generation efficiency. Notably, the unique energy transfer pathway effectively suppresses the generation of singlet oxygen ($^1O_2$), mechanistically circumventing the oxidative damage to small molecules and the formation of by-products commonly encountered in organic synthesis. Moreover, the selective oxidative activity of $O_2^{\bullet-}$ not only enables the visible-light-induced amidation of aromatic aldehydes with amines in an aqueous solution and a transition-metal-free system, providing an economical, green, and mild approach for amide bond formation, but also simultaneously achieves the oxidative dehydroaromatization of nitrogen-containing heterocycles (*e.g.*, tetrahydroquinolines and dihydroindoles), offering a universal strategy for the efficient synthesis of unsaturated nitrogen heterocyclic skeletons. This study has constructed an ordered multi-step energy transfer system with precise reactive oxygen species (ROS) regulation through supramolecular assembly, providing a reliable research paradigm for efficient light-to-chemical energy conversion and green organic synthesis.

Received 15th July 2025
Accepted 16th August 2025

DOI: 10.1039/d5sc05260b

rsc.li/chemical-science

Introduction

Photosynthesis is one of the most sophisticated energy conversion processes in nature. Through the synergistic action of Photosystem I (PSI) and Photosystem II (PSII), plants and photosynthetic microorganisms efficiently convert solar energy into chemical energy, providing an indispensable energy source for life on Earth.[1–4] The core of this process lies in a series of highly ordered energy transfer and electron transport steps, where light energy is first captured and converted into excited-state energy, which is then transferred through multiple steps to ultimately drive chemical reactions.[5–8] This multi-step, high-efficiency energy transfer mechanism not only demonstrates the exquisite design of nature but also provides significant inspiration for the development of artificial light-harvesting energy systems.[9–27]

Supramolecular chemistry, through non-covalent interactions such as electrostatic interactions, hydrogen bonding, and π–π stacking, enables precise molecular self-assembly and functional regulation, offering a powerful design platform for constructing complex functional systems.[28–35] Among these, electrostatic interactions, due to their tunable strength, directional specificity, and environmental responsiveness, have become one of the key driving forces in supramolecular assembly.[36–41] Based on this principle, sodium polystyrene sulfonate (RSS), an anionic polyelectrolyte with a specific structure, has shown remarkable application potential in the field of energy transfer due to its unique electrostatic properties and self-assembly capabilities.[42,43] RSS molecules can tightly bind with other functional molecules through electrostatic interactions, forming highly ordered composite structures. This binding not only provides a stable molecular platform for energy transfer but also optimizes the pathway and efficiency of energy transfer by precisely controlling the distance and orientation between molecules.[42,43]

School of Chemistry and Chemical Engineering, Shandong University of Technology, Zibo 255000, P. R. China. E-mail: liuwenqiang13@mail.ipc.ac.cn; lbxing@sdut.edu.cn

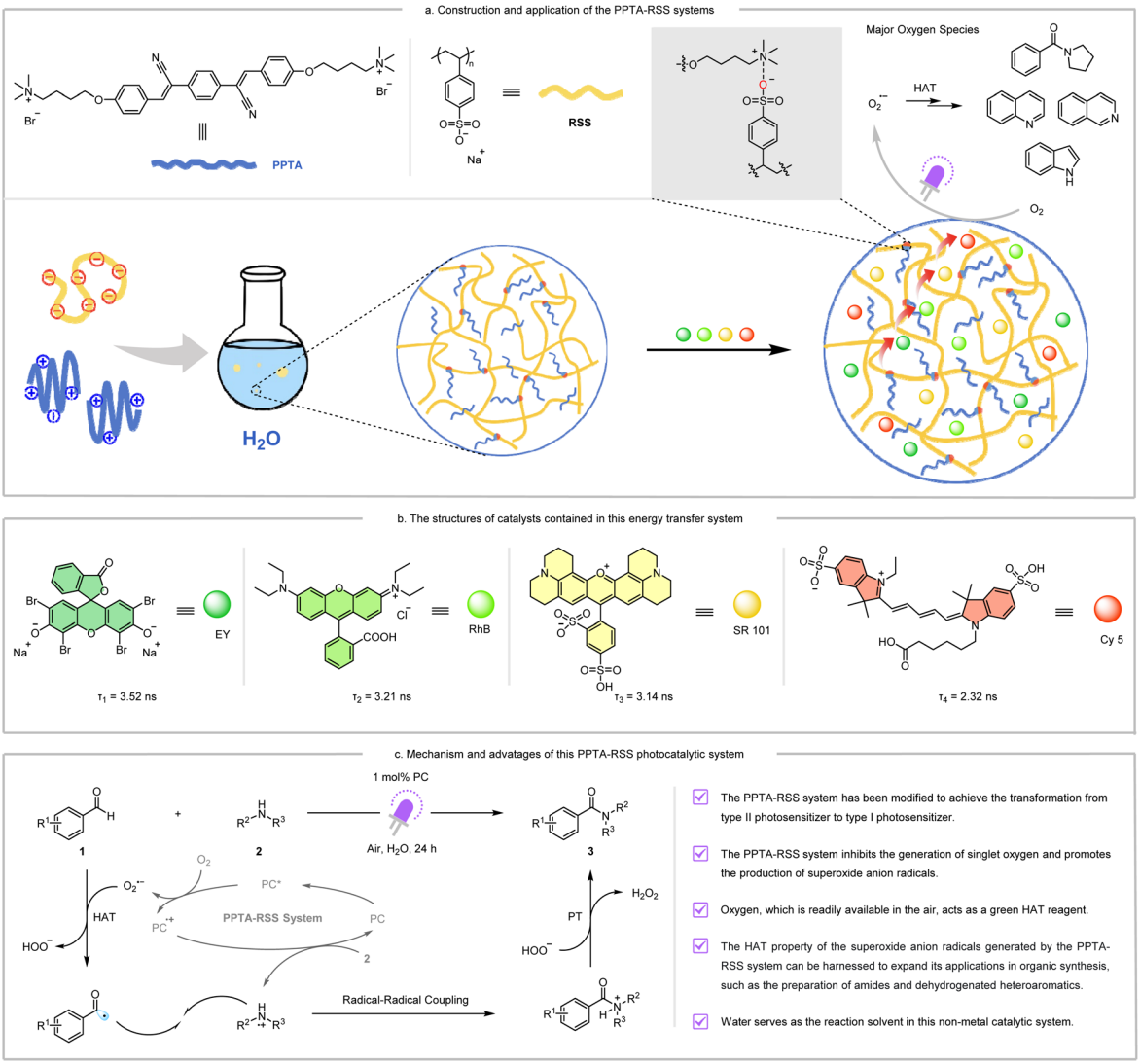

Scheme 1 (a) Construction and application of the PPTA-RSS systems; (b) the structures of catalysts contained in this energy transfer system; (c) mechanism and advantages of this PPTA-RSS photocatalytic system.

Despite the notable advancements in artificial light-harvesting systems, several critical challenges persist. First, the efficiency of single-step energy transfer remains inherently limited, rendering long-distance energy transmission particularly challenging. Second, substantial energy dissipation during multi-step transfer processes significantly restricts the overall efficiency.[44] Most importantly, the dysregulation of photo-induced reactive oxygen species (ROS)—notably singlet oxygen ($^1O_2$) and superoxide anion radical ($O_2^{\bullet-}$)—frequently compromises selectivity in organic synthesis. Mechanistically, $^1O_2$ mediates oxidative damage to small-molecule substrates, leading to the formation of complex by-product mixtures, while $O_2^{\bullet-}$ can serve as a highly effective oxidative driving force when its reactivity is directionally controlled.[45,46] Thus, the development of systems enabling ordered, efficient multi-step energy transfer with precise ROS regulation represents a frontier of both scientific and practical significance.

In this study, the polyelectrolyte RSS and the PPTA photocatalyst were closely combined through electrostatic interactions, successfully constructing a novel supramolecular-based energy-transfer system that achieved a continuous four-step energy-transfer process (Scheme 1a). In this system, energy is first transferred from the PPTA-RSS complex to the dye EY, and then sequentially to RhB, SR101, and Cy5. This step-by-step energy transfer leads to the rapid dissipation of excited-state energy, which is accompanied by a step-by-step decrease in fluorescence lifetime (Scheme 1b). Meanwhile, the generation of singlet oxygen ($^1O_2$) in the system is effectively inhibited, and the production efficiency of superoxide anion radicals ($O_2^{\bullet-}$) gradually increases. As the energy transfer progresses, the transformation from a type II photosensitizer to type I photosensitizer is accomplished. As shown in Scheme 1c, in the PPTA-RSS system, atmospheric oxygen acts as a green hydrogen atom transfer (HAT) reagent, and the generated $O_2^{\bullet-}$ effectively promotes the amidation of aromatic aldehydes with amines to

efficiently produce the corresponding amide products. Additionally, this system successfully achieves the oxidative dehydroaromatization of nitrogen-containing heterocycles. The use of water as the reaction solvent embodies green chemistry principles, further highlighting the advantages and synthetic potential of the PPTA-RSS photocatalytic system (Scheme 1a).

Results and discussion

The PPTA molecule was synthesized *via* a three-step reaction as depicted in Scheme S1 and characterized by ^{1}H NMR and ^{13}C NMR spectroscopy (Fig. S1 and S2). Initially, its spectral properties were investigated using UV-vis absorption and fluorescence emission spectroscopy. The results showed that PPTA exhibited an absorption band spanning 250–450 nm with a maximum absorption wavelength at 350 nm (Fig. 1a), and an emission band ranging from 400–700 nm with a maximum emission wavelength at 530 nm (Fig. 1b), displaying blue-green fluorescence in an aqueous solution (Fig. S3). Furthermore, the aggregation-induced emission (AIE) behavior of PPTA was studied by tuning its aggregation state in a H_2O-DMSO mixed solvent, where the poor solvent (H_2O) induced a transition from molecular monodispersion to aggregation. As shown in Fig. S4, PPTA displayed very weak emission in pure DMSO (5.0×10^{-5} M), while fluorescence emission gradually intensified with increasing water content (higher aggregation degree), confirming PPTA as a typical AIE-active molecule. To further regulate the aggregation behavior, an anionic polyelectrolyte RSS with opposite charge to PPTA was introduced, driving molecular assembly through electrostatic interactions. Upon gradual addition of RSS to the PPTA aqueous solution, electrostatic attraction promoted the transition of PPTA from monodispersion to aggregation, leading to a significant decrease in absorption peak intensity and a notable enhancement in fluorescence emission (Fig. 1a and b). The absorbance and fluorescence intensity stabilized after adding 300 μL of RSS, indicating the system reached equilibrium. The fluorescence lifetime increased from 4.05 ns to 4.21 ns, reflecting improved excited-state stability (Fig. 1c). Dynamic light scattering (DLS) results show that PPTA molecules exhibit a particle size concentrated around 200 nm, while, after forming the PPTA-RSS assembly, their particle size distribution significantly increases, centered at 400–600 nm, confirming the formation of large-sized aggregates (Fig. S5a and b). Transmission electron microscopy (TEM) analysis further revealed the morphological features of the assemblies. In the aqueous solution, PPTA molecules self-assembled into well-dispersed spherical structures with an average diameter of ~200 nm. Upon the introduction of the polyelectrolyte RSS, these spherical assemblies exhibited pronounced aggregation, forming irregular clusters composed of multiple spherical units, accompanied by a broadened size distribution (Fig. S5c and d). Concurrently, the zeta potential shifted from +14.0 mV to −14.2 mV (Fig. 1d), indicating that electrostatic interactions not only drive the aggregation process but also modulate the charge distribution and surface properties of the aggregates, thereby optimizing their optical performance and structural stability.

The AIE aggregates of PPTA induced by RSS exhibit significant fluorescence enhancement in aqueous media. The ordered conjugated structures and robust exciton couplings within these aggregates provide an excellent platform for the construction of artificial light-harvesting systems. We conducted an initial investigation into the Förster resonance energy transfer (FRET) mechanism between PPTA-RSS and EY. As illustrated in Fig. S6, the fluorescence emission spectra of PPTA-RSS precisely overlap with the UV-vis absorption profile of EY, which prompted the selection of EY as the primary energy acceptor. Fig. 2a shows a gradual decrease in the emission intensity of PPTA-RSS at 530 nm with increasing molar ratios. Concurrently, upon 350 nm excitation, a distinct emission band emerges at 560 nm, characteristic of EY. A stable equilibrium is achieved at a molar ratio of 1 : 0.075, accompanied by a notable transition in fluorescence color from green to bright yellow. The energy transfer efficiency (Φ_{ET}) and antenna effect (AE) at this optimal ratio are quantified at 44.38% and 8.74 (Fig. S10a), respectively. Meanwhile, the fluorescence quantum yield was measured to be 2.6% (Table S1). Time-resolved fluorescence spectroscopy (TRFS) measurements provide conclusive evidence for the FRET process. Specifically, the addition of 7.5% EY results in a pronounced reduction of the fluorescence lifetime of PPTA-RSS from 4.21 ns to 3.52 ns (Fig. 3c), unequivocally demonstrating the efficient transfer of excitation energy from PPTA-RSS to EY.

Based on the excellent overlapping characteristics between the UV-vis absorption spectra of RhB and the fluorescence emission spectra of PPTA-RSS + EY, we strategically selected RhB as the second energy acceptor (Fig. S7). As depicted in Fig. 2b, with the gradual addition of RhB, after the system was excited at 350 nm, the intensity of the emission band centered at 560 nm showed a decreasing trend. Meanwhile, the newly formed emission peak at 590 nm, which is attributed to RhB, was significantly enhanced. When the molar ratio of the system reached 1 : 0.075 : 0.090, the energy transfer process tended to be stable. At this time, the fluorescence color of the system changed from bright yellow to orange-yellow. Φ_{ET} and AE were measured to be 72.49% and 5.41, respectively (Fig. S10b), while the fluorescence quantum yield was 2.7% (Table S1). In addition, compared with the binary system of PPTA-RSS + EY, the introduction of RhB significantly shortened the fluorescence lifetime (3.21 ns). This result strongly supports the occurrence of a two-step sequential energy transfer process within the system.

Natural light-harvesting systems achieve efficient utilization of solar energy through a multi-step sequential energy transfer mechanism rather than a simple single-step or two-step transfer. Inspired by this, we further explored the feasibility of constructing a multi-step cascaded energy transfer system based on polyelectrolyte supramolecular scaffolds. Given the excellent overlap between the fluorescence emission spectra of PPTA-RSS + EY + RhB and the UV-vis absorption spectra of SR101 (Fig. S8), SR101 was selected as the third energy acceptor. When SR101 was gradually added to the PPTA-RSS + EY + RhB mixed solution system, under the excitation of 350 nm, the fluorescence emission intensity of RhB at 590 nm gradually decreased, while

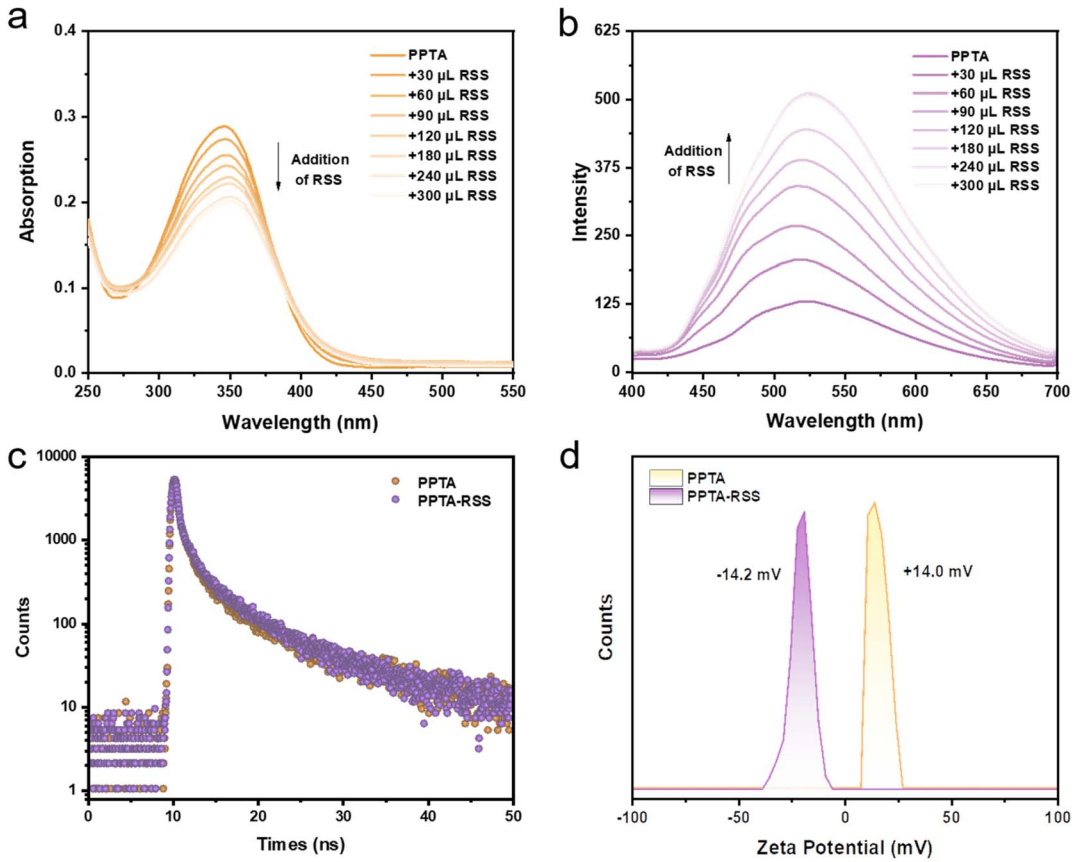

Fig. 1 (a) UV-vis absorption spectra changes of PPTA upon successive addition of RSS in H_2O; (b) fluorescence spectra changes of PPTA upon successive addition of RSS in H_2O (λ_{ex} = 350 nm); (c) time-resolved fluorescence spectroscopy of PPTA and PPTA-RSS; (d) zeta potentials of PPTA and PPTA-RSS. [PPTA] = 2.0×10^{-5} M, [RSS] = 3 μg L^{-1}.

the fluorescence signal of SR101 at 625 nm significantly increased (Fig. 2c). When the molar ratio of the system reached 1 : 0.075 : 0.090 : 0.12, the energy transfer process tended to be stable. The fluorescence color changed from orange-yellow to orange, and the corresponding Φ_{ET} and AE were stabilized at 53.58% and 13.83, respectively (Fig. S10c); the fluorescence quantum yield was measured to be 4.0% (Table S1). Fluorescence lifetime tests showed that after adding 12% of SR101, the fluorescence lifetime of the system decreased to 3.14 ns compared with the initial value, further confirming the occurrence of energy transfer.

Similarly, due to the high matching between the UV-vis absorption spectra of Cy5 and the fluorescence emission spectra of PPTA-RSS + EY + RhB + SR101 (Fig. S9), Cy5 was introduced as the fourth energy acceptor. After gradually adding Cy5 to the PPTA-RSS + EY + RhB + SR101 composite system, the fluorescence intensity of SR101 at 625 nm decreased as the concentration of Cy5 increased. At the same time, the fluorescence emission intensity of Cy5 at 700 nm increased gradually (Fig. 2d). When the molar ratio reached 1 : 0.075 : 0.090 : 0.12 : 0.10, the fluorescence color of the system changed from orange to orange-red. The Φ_{ET} and AE increased to 52.37% and 17.06, respectively (Fig. S10d), while the fluorescence quantum yield reached 6.0% (Table S1). Fluorescence lifetime analysis showed that after adding 10% of Cy5, the fluorescence lifetime of the system decreased significantly again (2.32 ns). This series of spectroscopic evidence jointly confirmed the successful construction of a four-step sequential energy transfer system based on polyelectrolyte scaffolds.

In photocatalytic reactions, singlet oxygen ($^1O_2$) and the superoxide anion radical ($O_2^{\bullet-}$) act as crucial reaction intermediates, and their generation efficiencies directly affect the progress of the catalytic reactions.[47–52] To study the dynamic changes of reactive oxygen species (ROS) in this assembled system under photoexcitation, 9,10-anthracenediyl-bis(methylene)-dimalonic acid (ABDA) and *N*,*N*,*N*′,*N*′-tetramethyl-1,4-phenylenediamine (TMPD) indicators were used to analyze the generation efficiencies of $^1O_2$ and $O_2^{\bullet-}$ respectively,[51,52] providing experimental evidence for revealing the mechanism of photocatalytic reactions. Studies reveal that PPTA molecules exhibit remarkable $^1O_2$ generation capability, which is further enhanced upon electrostatic assembly with the polyelectrolyte RSS to form a complex (Fig. S11). However, in a four-step sequential energy transfer system incorporating EY, RhB, SR101, and Cy5, the $^1O_2$ generation efficiency demonstrates a characteristic stepwise decline as energy transfers from the donor PPTA-RSS assembly to each acceptor molecule: a slight decrease occurs upon the first transfer to EY, followed

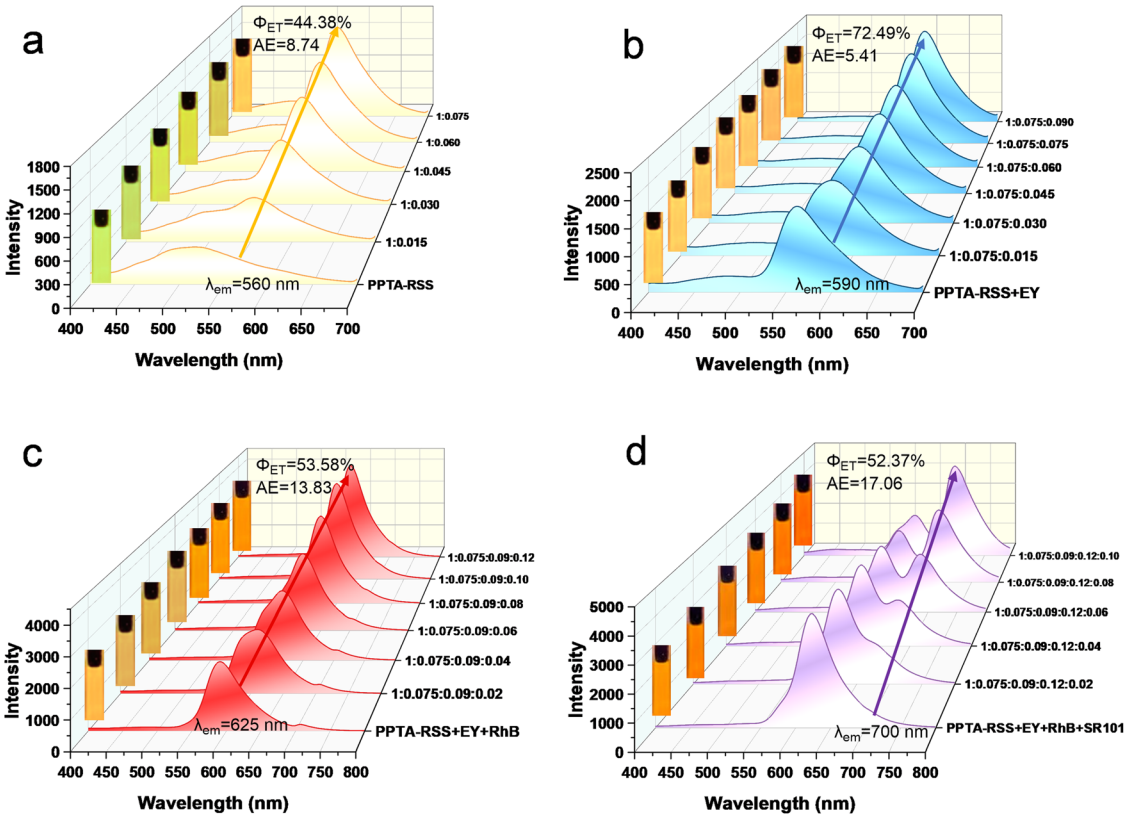

Fig. 2 (a) Fluorescence emission spectra of PPTA-RSS with gradual addition of EY, inset: fluorescence colors of PPTA-RSS before and after the addition of EY; (b) PPTA-RSS + EY with the gradual addition of RhB, inset: fluorescence colors of PPTA-RSS + EY before and after the addition of RhB; (c) PPTA-RSS + EY + RhB with the gradual addition of SR101, inset: fluorescence colors of PPTA-RSS + EY + RhB before and after the addition of SR101; (d) PPTA-RSS + EY + RhB + SR101 with the gradual addition of Cy5, inset: fluorescence colors of PPTA-RSS + EY + RhB + SR101 before and after the addition of Cy5. [PPTA] = 2.0×10^{-5} M, [RSS] = 3 μg L^{-1}.

by a significantly sharpened decline during the second transfer to RhB. Finally, when energy transferred from SR101 to the terminal acceptor Cy5, the efficiency of the generated $^1O_2$ was close to the background level of pure water (Fig. 3a and S11). In stark contrast to the attenuation of $^1O_2$, the generation efficiency of the superoxide anion radical ($O_2^{\bullet-}$) shows a continuous increasing trend throughout the supramolecular assembly and energy transfer processes (Fig. 3b). In addition, when the DMPO trapping agent was added to the PPTA-RSS + EY + RhB + SR101 + Cy5 solution, a distinct $O_2^{\bullet-}$ signal was detected after light irradiation (Fig. 3d). This inverse relationship in the generation efficiencies of $^1O_2$ and $O_2^{\bullet-}$ fundamentally arises from the dynamic competition between intermolecular electron transfer and energy transfer mechanisms during energy cascading. The PPTA-RSS assembly primarily generates $^1O_2$ *via* a type II mechanism (energy transfer), whereas as energy transfers to acceptor molecules with lower excited-state reduction potentials, the system gradually shifts to a dominant type I mechanism (electron transfer), where excited-state acceptors directly transfer electrons to ground-state oxygen molecules, promoting a stepwise increase in $O_2^{\bullet-}$ generation efficiency with each transfer stage. Such differential regulation of reactive oxygen species (ROS) generation provides critical mechanistic insights for the rational design of multifunctional photocatalytic systems based on energy transfer pathways.

Amides are crucial functional groups in natural compounds and are also widely applied in various industries such as polymers, pharmaceuticals, biomolecules, agrochemicals, *etc.*[53–58] Given the high efficiency driving role of $O_2^{\bullet-}$ in the oxidative amidation reactions of aldehydes, and considering the increasing characteristic of $O_2^{\bullet-}$ generation in the PPTA-RSS assembly energy transfer system revealed in previous studies, this research took benzaldehyde **1a** and pyrrolidine **2a** as model substrates to explore the performance of the photocatalytic oxidation reaction. Under standard reaction conditions, the isolated yield of the target product **3a** is 87% (Table 1, entry 1). Through a systematic investigation of the reaction parameters, it is found that when the energy transfer pathway is not established in the PPTA-RSS catalytic system (entry 2), the yield of the target product significantly decreases to 34%. This result directly demonstrates the crucial role of the energy transfer process in this catalytic system. When used individually, the catalytic activity of dye molecules was limited, with EY and RhB yielding the product at 16% and 28%, respectively, while SR101 and Cy5 produced only trace amounts. These results further highlight the superior efficiency and indispensable catalytic advantages of the PPTA-RSS photocatalyst in this reaction.

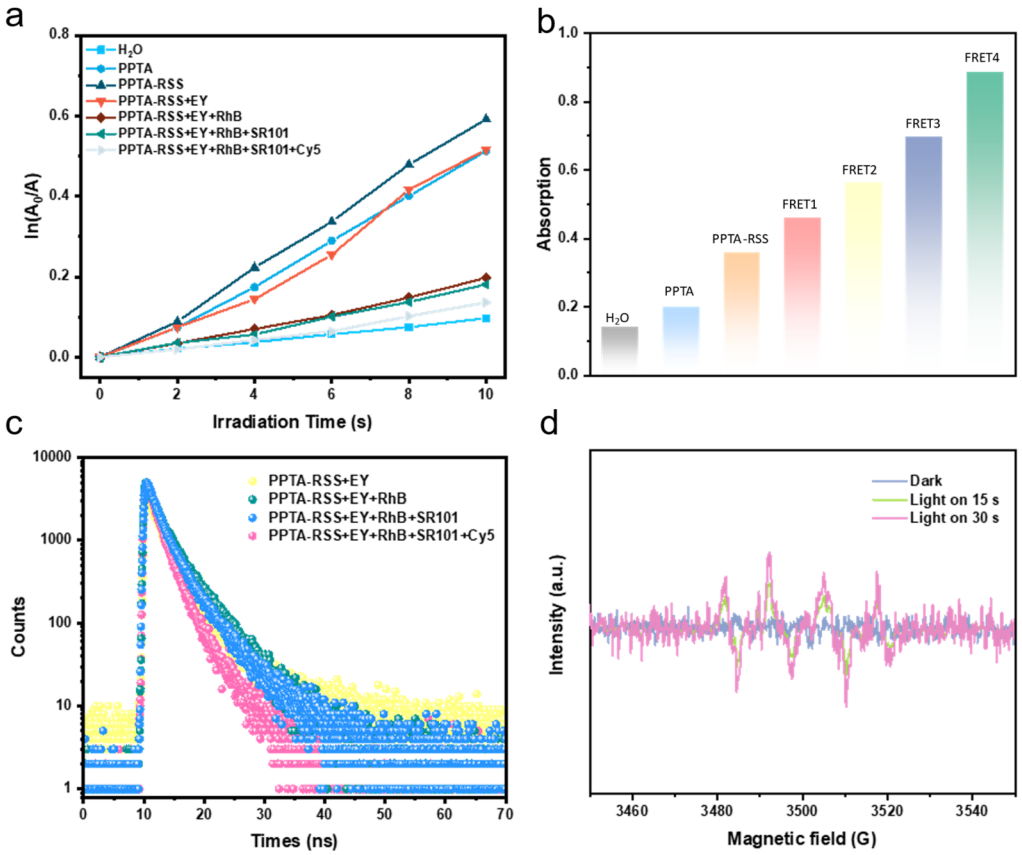

Fig. 3 (a) The time-dependent changes in the UV-vis absorption of ABDA at the wavelength of 378 nm in a series of PPTA system solutions for the generation of singlet oxygen ($^1O_2$) under light irradiation; (b) the time-dependent changes in the UV-vis absorption of TMPD in a series of PPTA system solutions for the generation of the superoxide radical ($O_2^{\bullet-}$) under light irradiation (FRET1: PPTA-RSS + EY; FRET2: PPTA-RSS + EY + RhB; FRET3: PPTA-RSS + EY + RhB + SR101; FRET4: PPTA-RSS + EY + RhB + SR101+Cy5); (c) time-resolved fluorescence spectroscopy of the energy transfer system; (d) the electron paramagnetic resonance (EPR) spectra of the superoxide radical ($O_2^{\bullet-}$) generated by the PPTA-RSS + EY + RhB + SR101 + Cy5 system in the presence of the spin-trapping agent DMPO under light irradiation [PPTA] = 2.0×10^{-5} M, [RSS] = 3 μg L^{-1}.

Furthermore, the catalytic efficiency of one-step, two-step, and three-step energy transfer systems is significantly lower than that of the PPTA-RSS system (entries 7–9), with their yields only being 43–56%. In addition, in the reaction system under a nitrogen atmosphere (entry 10), the formation of the target product is completely inhibited; while in a pure oxygen atmosphere (entry 11), the yield of the target product does not increase significantly. Benefiting from the absorption characteristics of PPTA molecules in the broad visible light spectrum, the change in the wavelength of light has a relatively limited impact on the catalytic performance (entries 12 and 13). Moreover, when neither light irradiation nor catalyst is present in the reaction system, no reaction is observed (entries 14 and 15). This result further confirms the indispensable roles of both light and the catalyst in the reaction process.

After determining the optimal reaction conditions, we systematically investigated the substrate scope. As shown in Table 2A, substrates featuring electron-withdrawing groups at the para position, including fluoro (**3b**), chloro (**3c**), bromo (**3d**), and nitro (**3e**) moieties, demonstrated remarkable reactivity. They were efficiently converted into the corresponding target products with high yields ranging from 84% to 89%. The 4-methyl substituted substrate (**3f**) also participated in the reaction, affording the product with a yield of 76%. Substrates with *ortho*-substituents, such as the methyl (**3g**) and fluoro (**3h**) derivatives, were also well-tolerated by the reaction system. These substrates provided products with moderately high yields, highlighting the influence of the substitution position on the reaction outcome. Moreover, when 4-pyridinecarboxaldehyde, a substrate containing a nitrogen-containing group, was employed (**3i**), an impressive yield of 82% was achieved. Significantly, the reaction system showed good adaptability to changes in the amine substrate. Under standard reaction conditions, the anticipated product was successfully obtained with a yield of 83% for substrate (**3j**). Overall, this reaction system exhibits broad applicability to substrates with diverse structural features. In addition, to demonstrate the practical applicability of the reaction, we scaled up the template reaction to the 10 mmol scale and prolonged the reaction time. The results showed that the target product was still obtained in a good yield of 72%.

Quinolines, as an important class of heterocyclic compounds, serve as the core structural unit of numerous natural products and hold critical application value in fields

Table 1 Optimization of amidation reaction conditions[a]

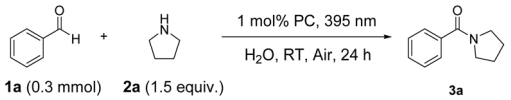

Entry	Deviation from standard conditions	Yield of **3a** (%)
1	None	87
2	PPTA-RSS instead of the PPTA-RSS system	34
3	EY instead of the PPTA-RSS system	16
4	RhB instead of the PPTA-RSS system	28
5	SR101 instead of the PPTA-RSS system	Trace
6	Cy5 instead of the PPTA-RSS system	Trace
7	PPTA-RSS + EY instead of the PPTA-RSS system	43
8	PPTA-RSS + EY + RhB instead of the PPTA-RSS system	48
9	PPTA-RSS + EY + RhB + SR101 instead of the PPTA-RSS system	56
10	N_2 instead of air	ND
11	O_2 instead of air	88
12	365 nm instead of 395 nm	89
13	425 nm instead of 395 nm	78
14	No light	ND
15	No PC	ND

[a] Standard conditions: benzaldehyde (0.3 mmol), pyrrolidine (0.45 mmol), PPTA-RSS + EY + RhB + SR101 + Cy5 (1 mol%), H_2O (2.0 mL), irradiated with a 395 nm LED at room temperature for 24 h. Yields were determined by isolated yield. PC, photocatalyst; RT, room temperature; ND, not detected.

such as antimalarial drugs and anticancer agents.[59,60] Based on this, this study further investigated the performance of the photocatalyst system (PPTA-RSS + EY + RhB + SR101 + Cy5) in the oxidative dehydroaromatization of nitrogen-containing heterocycles. Experimental results show (Table S2) that under standard reaction conditions, the isolated yield of the quinoline target product **5a** reaches 90%. Under standard reaction conditions, we conducted a systematic investigation of the substrate scope using a series of quinoline derivatives (Table 2B). The experimental results demonstrated that substrates bearing electron-withdrawing groups (such as fluoro, chloro, and bromo, **5b–5d**) on the aromatic ring all afforded excellent yields (76–87%). Notably, electron-donating groups such as methoxy and hydroxy (**5e** and **5f**) also displayed outstanding reactivity, providing the target products in high yields (88–91%). Of particular significance, we conducted an in-depth study on the positional effects of methyl substituents (**5g–5i**). The experimental data revealed a clear decreasing trend in yields (89–72%) as the methyl substitution position moved closer to the nitrogen-containing heterocycle (from the 6-position to the 2-position), unambiguously demonstrating the critical influence of steric effects on the reaction efficiency. Notably, even strongly electron-withdrawing nitro groups (**5j** and **5k**) exhibited good tolerance in this transformation, albeit with slightly diminished yields (57–60%). Remarkably, the catalytic system was not only applicable to quinoline substrates but also showed excellent compatibility with structurally analogous isoquinoline derivatives (**5l–5n**), maintaining high yields of 82–89%. Most encouragingly, the reaction system was successfully extended to five-membered nitrogen-containing heterocycles (**5o–5t**), all of which afforded the desired products in good yields. This important finding strongly attests to the broad applicability and synthetic potential of our developed methodology, offering a novel strategy for constructing diverse nitrogen-containing heterocyclic compounds.

The mechanistic investigation was conducted through a systematically designed series of control experiments, with the objective of identifying and characterizing the key reactive intermediates involved in the reaction pathway. In this study, KI, triethylamine (TEA), NaN_3, and *p*-benzoquinone (BQ) were selected as scavengers for photo-induced holes (h^+), hydroxyl radicals ($^{\bullet}OH$), singlet oxygen ($^1O_2$), and superoxide anion radicals ($O_2^{\bullet-}$), respectively.[61,62] The experimental data show that when TEA, KI, and NaN_3 were used as quenchers, there was no significant change in the yields of target products **3a** and **5a**. This indicates that the participation of hydroxyl radicals ($^{\bullet}OH$), photo-induced holes (h^+), and singlet oxygen ($^1O_2$) in this reaction can be neglected. It is worth noting that when *p*-benzoquinone (BQ) was introduced as a specific quencher for superoxide anion radicals ($O_2^{\bullet-}$), the yield of the target product **3a** and **5a** decreased dramatically to 19% and 26%, respectively (Fig. S13). This result directly proves that $O_2^{\bullet-}$ are the main reactive species driving the photocatalytic oxidation reaction. Based on the above quenching experiment results, this study proposes the following reaction mechanism. Upon 395 nm purple-light irradiation, the principal component [PPTA-RSS] within the PPTA-RSS composite photosensitizer is initially excited to a singlet state. Subsequently, it undergoes

Table 2 Substrate scope of the PPTA-RSS + EY + RhB + SR101 + Cy5-based photocatalytic aerobic oxidation for amidation/arylation reactions[a]

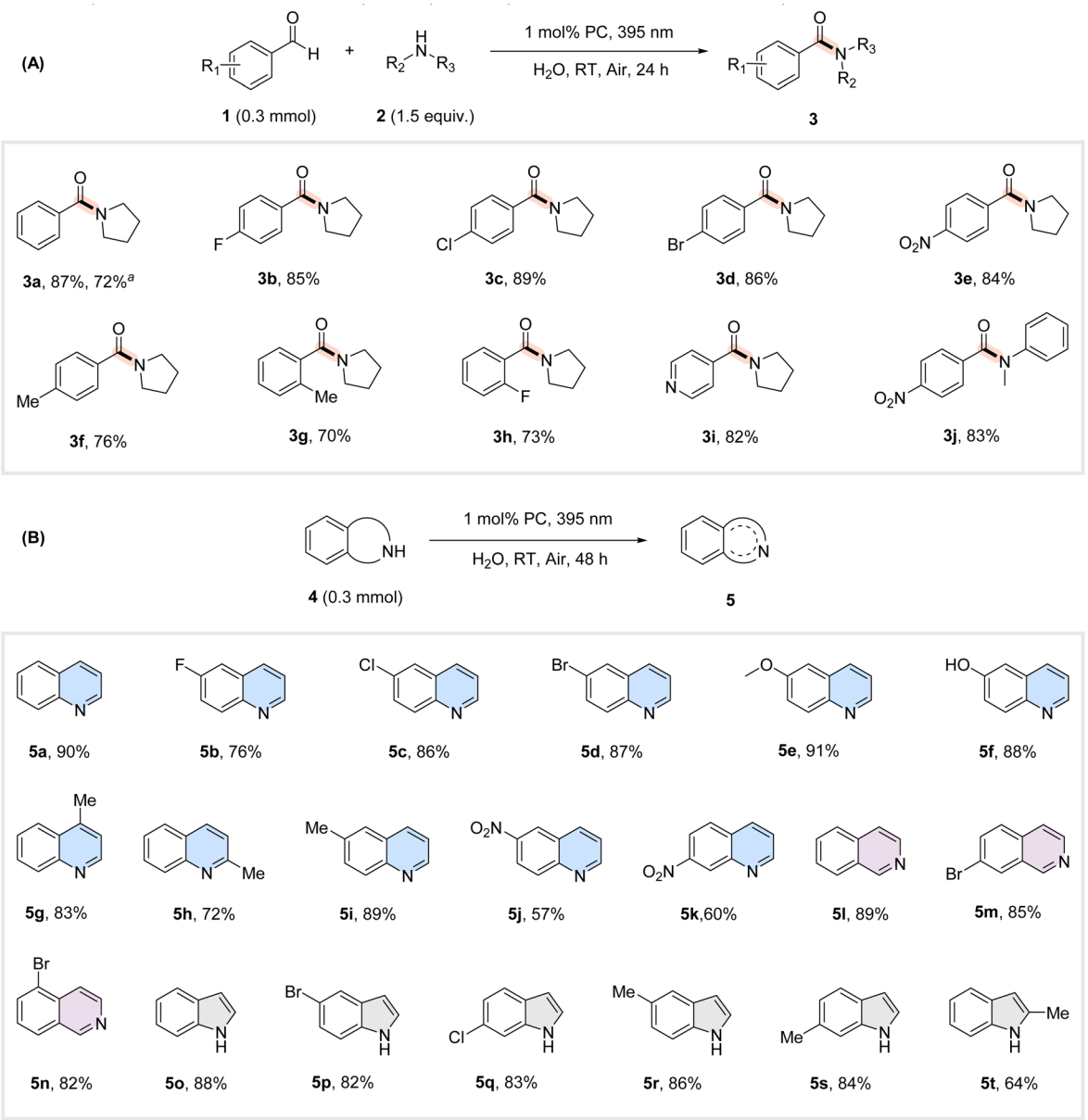

[a] Gram-scale reaction. (A) Standard conditions: benzaldehyde (0.3 mmol), pyrrolidine (0.45 mmol), PPTA-RSS + EY + RhB + SR101 + Cy5 (1 mol%), H_2O (2.0 mL), under air atmosphere, irradiated with a 395 nm LED at room temperature for 24 h. (B) Standard conditions: 1,2,3,4-tetrahydroquinoline (0.3 mmol), PPTA-RSS + EY + RhB + SR101 + Cy5 (1 mol%), H_2O (2.0 mL), under an air atmosphere, irradiated with a 395 nm LED at room temperature for 48 h.

intersystem crossing to yield a triplet excited state (^{3}[PPTA-RSS]). This excited state sequentially transfers energy to the acceptor dyes [EY], [RhB], and [SR101] *via* Förster resonance energy transfer (FRET), culminating in the formation of the excited state [Cy5] with potent reducing capabilities. [Cy5]* engages in photo-induced electron transfer (PET) with the ground-state triplet oxygen ($^3O_2$), giving rise to superoxide anion radicals ($O_2^{\bullet-}$) and cation radicals $[Cy5]^{\bullet+}$ (Scheme 2). The substrate benzaldehyde **1a** undergoes hydrogen atom transfer (HAT) with the superoxide radical anion ($O_2^{\bullet-}$) to yield radical intermediate I and the hydroperoxyl anion (HOO^-). Concurrently, pyrrolidine **2a** reduces $[Cy5]^{\bullet+}$ to the ground-state Cy5, with the concomitant generation of intermediate II during this process. Subsequent radical–radical coupling between intermediates I and II affords the pivotal intermediate III. Proton abstraction from intermediate III by the hydroperoxyl anion (HOO^-) ultimately leads to the formation of hydrogen peroxide concomitant with the target product **3a**. The formation of

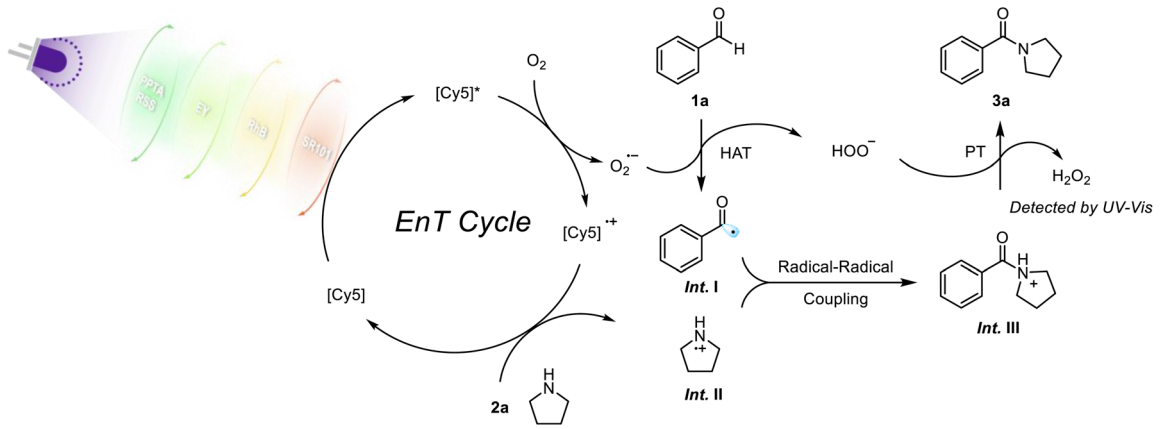

Scheme 2 Proposed mechanism for the photocatalytic oxidative amidation reaction.

hydrogen peroxide in this photocatalytic system has been conclusively verified by the $Ce(SO_4)_2$ colorimetric method in conjunction with UV-vis spectroscopy (Fig. S12). In addition, the mechanism of photocatalytic oxidative arylation is described in detail in the SI (Scheme S1).

Conclusion

In this study, a four-step energy transfer supramolecular platform based on sodium polystyrene sulfonate (RSS) and a quaternary ammonium salt-modified styrene derivative (PPTA) was successfully constructed *via* the electrostatic supramolecular assembly strategy. This system has broken through the technical bottlenecks of low-efficiency long-distance energy transmission and fixed single-step transfer distance in artificial light-harvesting systems, achieving efficient directional energy relay from the PPTA-RSS complex to EY, RhB, SR101, and Cy5. The unique energy transfer pathway not only effectively suppresses the generation of $^1O_2$ but also significantly enhances the yield of superoxide anion radicals ($O_2^{\bullet-}$), providing a strong oxidative driving force for photocatalytic reactions. This system enables not only the visible-light-mediated amidation of aromatic aldehydes with amines under aqueous and transition-metal-free conditions but also the oxidative dehydroaromatization of nitrogen-containing heterocycles. These findings not only provide key scientific evidence for revealing the dynamic regulation rules of multi-step energy transfer and conversion but also open up a new path of the energy cascade strategy for the green synthesis of complex organic molecules through the precise regulation of visible-light-induced reactive oxygen species.

Author contributions

Y.-S. B. constructed and characterized the molecular assemblies, constructed the light-harvesting systems, synthesized all the substrates and performed the photophysical measurements. W.-Q. L. investigated the reaction mechanism and wrote the manuscript. H. L. revised the manuscript. L.-B. X. designed the work, provided intellectual input, and wrote and revised the manuscript.

Conflicts of interest

The authors declare no conflict of interest.

Data availability

All the data supporting this article have been included in the main text and the SI.

Experimental method including materials, characterizations, synthetic route, energy-transfer efficiency calculation, antenna effect calculation, detection of ROS, gram-scale experiments, detection of H_2O_2, and spectroscopic data, SI figures and tables, NMR spectra can be found in the SI. See DOI: **https://doi.org/10.1039/d5sc05260b**.

Acknowledgements

We are grateful for the financial support from the National Natural Science Foundation of China (52205210) and the Natural Science Foundation of Shandong Province (ZR2022QE033).

Notes and references

1 H.-Q. Peng, L.-Y. Niu, Y.-Z. Chen, L.-Z. Wu, C.-H. Tung and Q.-Z. Yang, *Chem. Rev.*, 2015, **115**, 7502–7542.
2 G. McDermott, S. M. Prince, A. A. Freer, A. M. Hawthornthwaite-Lawless, M. Z. Papiz, R. J. Cogdell and N. W. Isaacs, *Nature*, 1995, **374**, 517–521.
3 A. M. van Oijen, M. Ketelaars, J. Köhler, T. J. Aartsma and J. Schmidt, *Science*, 1999, **285**, 400–402.
4 G. D. Scholes, G. R. Fleming, A. Olaya-Castro and R. van Grondelle, *Nat. Chem.*, 2011, **3**, 763–774.
5 H.-Q. Peng, Y.-Z. Chen, Y. Zhao, Q.-Z. Yang, L.-Z. Wu, C.-H. Tung, L.-P. Zhang and Q.-X. Tong, *Angew. Chem., Int. Ed.*, 2012, **51**, 2088–2092.
6 S. Kundu and A. Patra, *Chem. Rev.*, 2017, **117**, 712–757.

7 K. Wang, K. Velmurugan, B. Li and X.-Y. Hu, *Chem. Commun.*, 2021, **57**, 13641–13654.
8 O. Dumele, J. Chen, J. V. Passarelli and S. I. Stupp, *Adv. Mater.*, 2020, **32**, 1907247.
9 J.-J. Li, Y. Chen, J. Yu, N. Cheng and Y. Liu, *Adv. Mater.*, 2017, **29**, 1701905.
10 Z. Zhang, Z. Zhao, Y. Hou, H. Wang, X. Li, G. He and M. Zhang, *Angew. Chem., Int. Ed.*, 2019, **58**, 8862–8866.
11 Y. Li, Y. Dong, L. Cheng, C. Qin, H. Nian, H. Zhang, Y. Yu and L. Cao, *J. Am. Chem. Soc.*, 2019, **141**, 8412–8415.
12 C. Vijayakumar, K. Sugiyasu and M. Takeuchi, *Chem. Sci.*, 2011, **2**, 291–294.
13 Y. Liu, J. Jin, H. Deng, K. Li, Y. Zheng, C. Yu and Y. Zhou, *Angew. Chem., Int. Ed.*, 2016, **55**, 7952–7957.
14 L. Xu, Z. Wang, R. Wang, L. Wang, X. He, H. Jiang, H. Tang, D. Cao and B. Z. Tang, *Angew. Chem., Int. Ed.*, 2020, **59**, 9908–9913.
15 X.-M. Chen, Q. Cao, H. K. Bisoyi, M. Wang, H. Yang and Q. Li, *Angew. Chem., Int. Ed.*, 2020, **59**, 10493–10497.
16 H.-J. Kim, D. R. Whang, J. Gierschner and S. Y. Park, *Angew. Chem., Int. Ed.*, 2016, **55**, 15915–15919.
17 S. Guo, Y. Song, Y. He, X.-Y. Hu and L. Wang, *Angew. Chem., Int. Ed.*, 2018, **57**, 3163–3167.
18 Z. Lian, J. He, L. Liu, Y. Fan, X. Chen and H. Jiang, *Nat. Commun.*, 2023, **14**, 2752.
19 K. Acharyya, S. Bhattacharyya, S. Lu, Y. Sun, P. S. Mukherjee and P. J. Stang, *Angew. Chem., Int. Ed.*, 2022, **61**, e202200715.
20 Y. Han, X. Zhang, Z. Ge, Z. Gao, R. Liao and F. Wang, *Nat. Commun.*, 2022, **13**, 3546.
21 T. Xiao, L. Zhang, H. Wu, H. Qian, D. Ren, Z.-Y. Li and X.-Q. Sun, *Chem. Commun.*, 2021, **57**, 5782–5785.
22 M. Suresh, A. K. Mandal, E. Suresh and A. Das, *Chem. Sci.*, 2013, **4**, 2380–2386.
23 R. Cen, M. Liu, J.-H. Lu, Z. Tao and X. Xiao, *ACS Appl. Mater. Interfaces*, 2024, **16**, 13132–13138.
24 Q. Song, S. Goia, J. Yang, S. C. L. Hall, M. Staniforth, V. G. Stavros and S. Perrier, *J. Am. Chem. Soc.*, 2021, **143**, 382–389.
25 M. Hao, G. Sun, M. Zuo, Z. Xu, Y. Chen, X.-Y. Hu and L. Wang, *Angew. Chem., Int. Ed.*, 2020, **59**, 10095–10100.
26 Y. Li, C. Xia, R. Tian, L. Zhao, J. Hou, J. Wang, Q. Luo, J. Xu, L. Wang, C. Hou, B. Yang, H. Sun and J. Liu, *ACS Nano*, 2022, **16**, 8012–8021.
27 D. Zhang, W. Yu, S. Li, Y. Xia, X. Li, Y. Li and T. Yi, *J. Am. Chem. Soc.*, 2021, **143**, 1313–1317.
28 S. Chen, P. Slattum, C. Wang and L. Zang, *Chem. Rev.*, 2015, **115**, 11967–11998.
29 Y. Jiao, K. Liu, G. Wang, Y. Wang and X. Zhang, *Chem. Sci.*, 2015, **6**, 3975–3980.
30 H. Wang, K.-F. Xue, Y. Yang, H. Hu, J.-F. Xu and X. Zhang, *J. Am. Chem. Soc.*, 2022, **144**, 2360–2367.
31 M. Hecht, P. Leowanawat, T. Gerlach, V. Stepanenko, M. Stolte, M. Lehmann and F. Würthner, *Angew. Chem., Int. Ed.*, 2020, **59**, 17084–17090.
32 T. Seki, S. Yagai, T. Karatsu and A. Kitamura, *J. Org. Chem.*, 2008, **73**, 3328–3335.
33 S. T. J. Ryan, J. Del Barrio, I. Ghosh, F. Biedermann, A. I. Lazar, Y. Lan, R. J. Coulston, W. M. Nau and O. A. Scherman, *J. Am. Chem. Soc.*, 2014, **136**, 9053–9060.
34 Z. Wu, H. Qian, X. Li, T. Xiao and L. Wang, *Chin. Chem. Lett.*, 2023, **35**, 108829.
35 Q. Zhang, X. Dang, F. Cui and T. Xiao, *Chem. Commun.*, 2024, **60**, 10064–10079.
36 Y.-Y. Hu, X.-Y. Dai, X. Dong, M. Huo and Y. Liu, *Angew. Chem., Int. Ed.*, 2022, **61**, e202213097.
37 D. Li, Y. Yang, J. Yang, M. Fang, B. Z. Tang and Z. Li, *Nat. Commun.*, 2022, **13**, 347.
38 F. Lin, H. Wang, Y. Cao, R. Yu, G. Liang, H. Huang, Y. Mu, Z. Yang and Z. Chi, *Adv. Mater.*, 2022, **34**, 2108333.
39 H.-J. Wang, W.-W. Xing, Z.-H. Yu, H.-Y. Zhang, W.-W. Xu and Y. Liu, *Adv. Opt. Mater.*, 2022, **10**, 2201903.
40 H. Peng, G. Xie, Y. Cao, L. Zhang, X. Yan, X. Zhang, S. Miao, Y. Tao, H. Li, C. Zheng, W. Huang and R. Chen, *Sci. Adv.*, 2022, **8**, eabk2925.
41 P.-P. Jia, L. Xu, Y.-X. Hu, W.-J. Li, X.-Q. Wang, Q.-H. Ling, X. Shi, G.-Q. Yin, X. Li, H. Sun, Y. Jiang and H.-B. Yang, *J. Am. Chem. Soc.*, 2021, **143**, 399–408.
42 R.-Z. Zhang, H. Liu, C.-L. Xin, N. Han, C.-Q. Ma, S. Yu, Y.-B. Wang and L.-B. Xing, *J. Colloid Interface Sci.*, 2023, **651**, 894–901.
43 C.-Q. Ma, X.-L. Li, N. Han, Y. Wang, R.-Z. Wang, S. Yu, Y.-B. Wang and L.-B. Xing, *J. Mater. Chem. A*, 2022, **10**, 16390–16395.
44 G.-L. Li, K.-K. Niu, X.-Z. Yang, H. Liu, S. Yu and L.-B. Xing, *J. Mater. Chem. A*, 2024, **12**, 13356–13363.
45 C. S. Foote, *Science*, 1968, **162**, 963–970.
46 D. R. Kearns, *Chem. Rev.*, 1971, **71**, 395–427.
47 Q. Zhou, G. Huang, J. Si, Y. Wu, S. Jin, Y. Ji and Z. Ge, *ACS Nano*, 2024, **18**, 35671–35683.
48 X. Zhan, Y. Jin, C. Qu, H. Liu, R. Jiang, Q. Zhi, D. Qi, K. Wang, B. Han, H. Pan and J. Jiang, *Adv. Funct. Mater.*, 2025, **35**, 2415629.
49 Y. Yue, B. Li, D. Wang, C. Wu, Z. Li and B. Liu, *Adv. Funct. Mater.*, 2025, **35**, 2414542.
50 Y.-S. Bi, R.-Z. Zhang, K.-K. Niu, H. Liu and L.-B. Xing, *Org. Chem. Front.*, 2025, **12**, 3363–3372.
51 K.-K. Niu, T.-X. Luan, J. Cui, H. Liu, L.-B. Xing and P.-Z. Li, *ACS Catal.*, 2024, **14**, 2631–2641.
52 S. Yu, R.-X. Zhu, K.-K. Niu, N. Han, H. Liu and L.-B. Xing, *Chem. Sci.*, 2024, **15**, 1870–1878.
53 S. Das, S. Mondal, S. P. Midya, S. Mondal, E. Ghosh and P. Ghosh, *J. Org. Chem.*, 2023, **88**, 14847–14859.
54 S. Gaspa, A. Farina, M. Tilocca, A. Porcheddu, L. Pisano, M. Carraro, U. Azzena and L. De Luca, *J. Org. Chem.*, 2020, **85**, 11679–11687.
55 V. Vyas, V. Kumar and A. Indra, *Chem. Commun.*, 2024, **60**, 2544–2547.
56 J. Kweon, B. Park, D. Kim and S. Chang, *Nat. Commun.*, 2024, **15**, 3788.
57 X. Chen, Z. Lian and S. Kramer, *Angew. Chem., Int. Ed.*, 2023, **62**, e202217638.
58 J. Liu, C. Zhang, Z. Zhang, X. Wen, X. Dou, J. Wei, X. Qiu, S. Song and N. Jiao, *Science*, 2020, **367**, 281–285.

59 R. S. Keri and S. A. Patil, *Biomed. Pharmacother.*, 2014, **68**, 1161–1175.
60 K. Sun, H. Shan, R. Ma, P. Wang, H. Neumann, G.-P. Lu and M. Beller, *Chem. Sci.*, 2022, **13**, 6865–6872.
61 X. Zhan, Y. Wang, C. Sun, Y. Fang, L. Huang, Z. Ullah, Q. Chen, X. Wang, Z. Xing and G. Ouyang, *Adv. Sci.*, 2025, **12**, 2502342.
62 M.-H. Li, Z. Yang, H. Hui, Y. Wang, B. Yang, Z. Zhang and Y.-W. Yang, *Nano Lett.*, 2025, **25**, 7524–7532.